RSC Advances

PAPER

View Article Online
View Journal | View Issue

Cite this: *RSC Adv.*, 2026, **16**, 17184

A terahertz metamaterial-based approach for detecting trace 1-naphthaleneacetic acid residues *via* AOO-optimized support vector regression

Xiaodong Mao, Zhikai Huang, Tao Yang and Jun Hu *

Excessive residues of 1-naphthaleneacetic acid (NAA) pose a potential threat to people's health. This research aims to develop a highly sensitive method for detecting NAA residues. By integrating terahertz metamaterial sensors with intelligent optimization algorithms, it is intended to achieve rapid and accurate detection of trace amounts of NAA. A terahertz metamaterial sensor based on a composite dual-peak structure with L-shaped resonant elements is introduced. Spectral data of different concentrations of NAA solutions were collected using terahertz time-domain spectroscopy (THz-TDS), and Animated Oat Optimization (AOO) was used to optimize the hyperparameters of the support vector regression (SVR) model, thereby constructing an AOO-SVR quantitative prediction model. Furthermore, by optimizing the spectral data dimension through five feature extraction algorithms, the model performance was further enhanced. The results showed that the RFE-AOO-SVR model performed the best in terms of prediction accuracy, with a correlation coefficient (R) of 0.9715 and a limit of detection (LOD) of 0.036 μg mL^{-1}. This study verified the effectiveness of terahertz metamaterial sensors combined with intelligent optimization algorithms in the detection of NAA residues, providing a new method for the rapid quantitative analysis of pesticide residues.

Received 13th January 2026
Accepted 18th February 2026

DOI: 10.1039/d6ra00316h

rsc.li/rsc-advances

1 Introduction

1-Naphthaleneacetic acid (NAA) is an artificially synthesized plant growth regulator, widely used in agricultural production. It is mainly employed to promote plant growth, regulate physiological metabolic processes, and increase crop yields. NAA belongs to the auxin class of substances. Its mechanism of action mainly involves mimicking the functions of natural auxin (IAA), promoting plant cell elongation, inducing the formation of adventitious roots, and to some extent, delaying fruit abscission. In fruit tree cultivation, NAA is often used for fruit preservation, promoting root formation of cuttings, extending the harvest period, *etc.*, which helps to improve the commercial value and storage stability of crops.[1–3] However, as an artificially synthesized plant hormone, NAA can easily leave residues on the surface or tissues of fruits and vegetables if used improperly or with excessive dosage. Long-term consumption may have an impact on human health. Although the toxicity of NAA is relatively low, studies have shown that it may have potential reproductive toxicity, endocrine disruption effects, and adverse effects on liver and kidney functions.[4–6] Therefore, many countries and regions have set strict maximum residue limits for NAA in agricultural products to ensure food safety. For example, in China's "GB 2763-2021 Maximum Residue Limits for Pesticides in Food", it is stipulated that the maximum residue of NAA in apples is 0.1 mg kg^{-1}.[7] Since NAA usually exists on the surface of fruits and vegetables at a low concentration, its detection faces technical challenges such as insufficient sensitivity and selectivity. Therefore, developing a simple, rapid, accurate, and highly sensitive NAA residue detection technology is of great practical significance for ensuring food safety and public health.

Terahertz waves (THz) typically refer to electromagnetic waves with a frequency range of 0.1 to 10 THz, lying between microwaves and infrared. They represent an underutilized part of the electromagnetic spectrum and are thus also known as the "Terahertz void" or the "intersection point of electronics and photonics".[8,9] With the advancements in materials science, microelectronics technology, and laser devices, terahertz technology has experienced rapid development in recent years and has shown great potential in non-destructive testing, biological imaging, security inspection, communication, and spectral analysis. It has significant advantages in terms of high sensitivity, non-contact, and strong penetration, making it one of the important research directions in current cutting-edge interdisciplinary science. Compared to visible light and infrared light, terahertz waves have excellent penetration properties for non-polar materials (such as plastics, paper, wood, ceramics, textiles, *etc.*), enabling imaging and detection of the internal structure of non-metallic or low-humidity materials.[10–12]

School of Mechatronics & Vehicle Engineering, East China Jiaotong University, Nanchang, Jiangxi, 330013, PR China. E-mail: hujun_ecjtu@163.com

Therefore, terahertz technology has unique advantages in non-destructive testing and security inspection.

Metamaterials are a class of artificial materials that achieve specific electromagnetic responses by artificially designing and periodically constructing microscopic structural units. Their properties do not originate from the intrinsic attributes of the constituent materials but are determined by their geometric structures and arrangement patterns. Compared with natural materials, metamaterials can exhibit a series of unconventional optical phenomena such as negative refractive index, superlens effect, electromagnetic shielding, and perfect absorption within specific frequency bands, thereby enabling precise control over the propagation of electromagnetic waves. Particularly in the terahertz band, metamaterials, due to their size structures matching the wavelength, can effectively enhance the local electric field and improve the coupling efficiency with substances, becoming one of the key means to enhance the functional performance of terahertz waves. In terahertz detection, metamaterials enhance the absorption or transmission response at specific frequencies through resonant structures, significantly improving the system's ability to detect weak signals and detection sensitivity.[13–15] Ahmed F. *et al.*[16] designed a magnetic resonance sensor with a high absorption rate of 99.43% at the resonance frequency, which was used for the detection of trace pesticide residues. Chowdhury *et al.*[17] designed a new type of metamaterial (MS) sensor with a refractive index (RI) sensitivity of 0.125 THz per RIU, a quality factor of 5.262 and 4.084, for the detection of imidacloprid. Du X. *et al.*[18] designed a dual-peak flexible metamaterial composed of a rectangular ring and a rectangular planar array, with absorption rates of 94.06% and 97.07% respectively, achieving high sensitivity detection of fipronil with a detection limit of 0.01 mg L^{-1}. All these studies have shown that metamaterials have good feasibility in pesticide residue detection.

2 Experimental sample preparation and simulation results

2.1 Preparation of experimental samples

2.1.1 Design and simulation of metamaterials. In this work, the structural model of the proposed metamaterial sensor was established using Lumerical FDTD solutions. The geometric configuration of the L-type resonant elements is illustrated in Fig. 1: Period P_1: 58 μm; L_1: 32 μm; L_2: 22 μm; L_3: 17 μm; L_4: 14 μm; L_5: 4 μm; W_1: 2 μm; W_2: 4 μm. The base material of the structure is selected as silicon with a refractive index of 3.335, and the surface metal layer is gold, which is used to enhance the resonance response characteristics of the terahertz band.

In FDTD, the L-type resonant terahertz metamaterial sensor structure was simulated. Fig. 2 illustrates the terahertz transmission response of the L-type resonant structure. According to the spectra, the metamaterial sensor produces two notable resonance peak in the terahertz region at 2.13 THz and 2.70 THz.

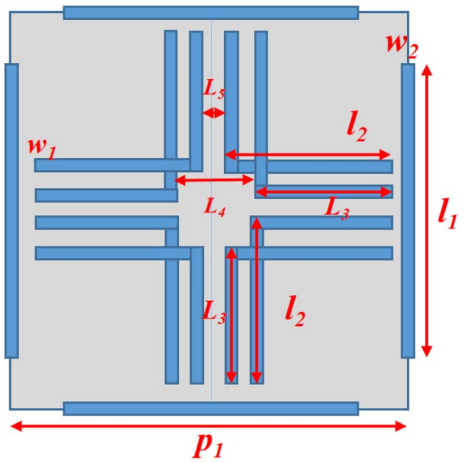

Fig. 1 Geometric parameters of the metamaterial sensor.

In the design and performance evaluation of metamaterial structures, the quality factor (*Q*-factor) and sensitivity (*S*) are commonly extracted from simulated spectral responses as key performance metrics, and they are employed to determine the optimal structural parameters. The *Q*-factor is defined as the ratio of the resonance frequency f_0 to the corresponding full width at half maximum (FWHM), reflecting the sharpness of the resonance peak and the energy loss characteristics of the system. A higher *Q*-factor indicates a narrower resonance bandwidth and higher frequency resolution, which is beneficial for enhancing localized electric fields and improving sensing performance.

According to the simulation results, the FWHM values of the two resonance modes f_1 and f_2 are 132 GHz and 636 GHz, respectively, resulting in *Q*-factors of 15.9 and 4.29. Sensitivity (*S*) is used to quantify the response of the structure to variations in environmental parameters and is typically defined as the ratio of the resonance frequency shift Δf to the refractive index change Δn, with the unit of GHz per RIU. When the surrounding refractive index increases from 1.2 to 2.0, the resonance frequencies f_1 and f_2 exhibit shifts of 26.7 GHz and 80 GHz,

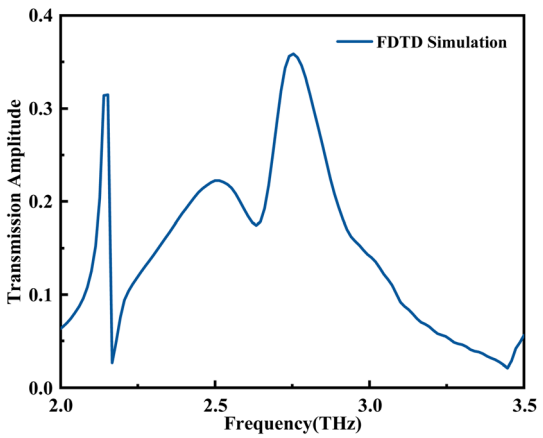

Fig. 2 FDTD simulation results.

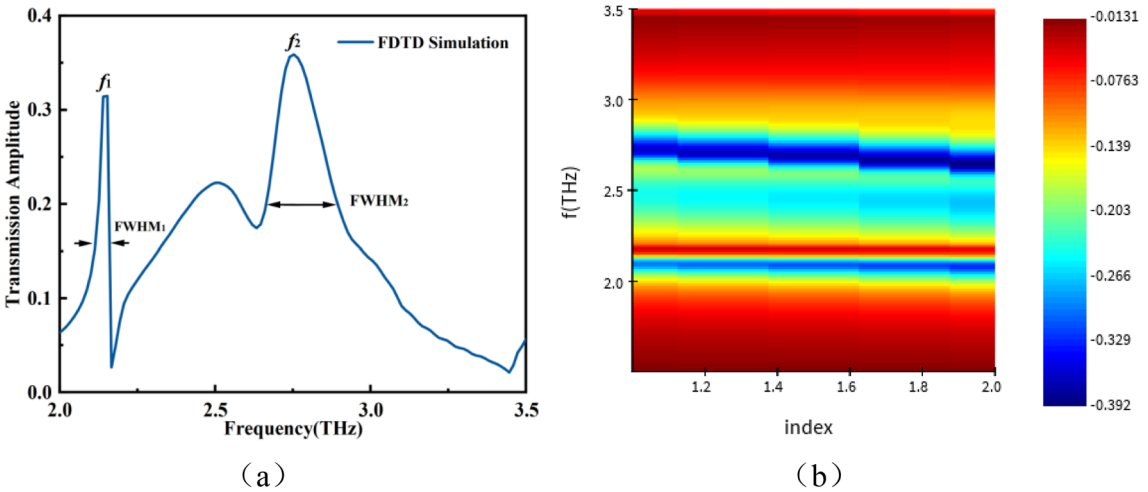

Fig. 3 Calculation of metamaterial performance metrics: (a) schematic of FWHM; (b) resonance frequency shift.

respectively, corresponding to sensitivities of 33.4 GHz per RIU and 100 GHz per RIU, demonstrating that the proposed structure possesses a favorable response to refractive index perturbations. Fig. 3 shows the calculation of the metamaterial performance metrics, including the FWHM evaluation and resonance frequency shift.

The L-type resonant metamaterial was fabricated using standard micro–nano fabrication techniques. High-resistivity silicon wafers with polished surfaces were selected as the substrates and sequentially cleaned using organic solvents and deionized water to remove surface contaminants. An oxygen plasma treatment was subsequently applied to improve surface hydrophilicity and enhance the adhesion of the photoresist layer. A thin adhesion layer of chromium (approximately 5 nm) was first deposited onto the silicon substrate, followed by the deposition of a metallic layer with a thickness of about 100 nm using electron-beam evaporation (or magnetron sputtering). The patterned resonant structures were defined by photolithography. A positive photoresist was spin-coated at a rotation speed of approximately 3000 rpm to obtain a uniform resist film with a thickness of about 1–2 μm, followed by soft baking at 10 °C for 2 min to remove residual solvent.

After ultraviolet exposure through a designed photomask, the sample was developed to form the L-shaped resonant patterns. The exposed metal layer was then transferred using reactive ion etching (RIE) or ion beam etching (IBE). Finally, the remaining photoresist was removed by acetone-assisted ultrasonic cleaning, leaving the well-defined metallic resonator array on the silicon substrate.

To ensure structural integrity and electrical performance, post-fabrication treatments such as surface oxidation or additional metal coating were applied when necessary. The photograph and scanning electron microscopy (SEM) images of the fabricated metamaterial are shown in Fig. 4.

The proposed L-shaped metamaterial unit intentionally introduces intrinsic geometric asymmetry, which enables the excitation of two distinct coupled resonance modes within a single-layer resonator. Unlike conventional symmetric

Fig. 4 (a) Photograph of the metamaterial; (b) SEM image of the metamaterial.

Table 1 Gradient table of NAA solution concentration

Serial number	Solution concentration ($\mu g\ mL^{-1}$)	Serial number	Solution concentration ($\mu g\ mL^{-1}$)	Serial number	Solution concentration ($\mu g\ mL^{-1}$)
1	0.01	6	0.06	11	0.11
2	0.02	7	0.07	12	0.12
3	0.03	8	0.08	13	0.13
4	0.04	9	0.09	14	0.14
5	0.05	10	0.10	15	0.15

structures or multimode designs based on multiple resonators, the dual-mode response here originates from the internal coupling mechanism of a single asymmetric unit. The two resonance modes exhibit different sensitivities to dielectric perturbations, providing complementary spectral features that are beneficial for quantitative sensing and regression modeling.

2.1.2 NAA sample preparation. In this work, 15 gradient concentrations were formulated through a sequential dilution approach. The stock standard was precisely brought to the required concentration using ultrapure water and a calibrated micropipette. Each diluted level was then homogenized with a vortex mixer to ensure uniform dispersion of the solute. The resulting mixtures were placed in light-shielding amber containers and kept airtight to prevent degradation. An overview of the concentration levels is provided in Table 1.

2.2 Spectral acquisition

Before the formal measurements, the spectrometer's optical cavity was purged with dry air supplied by an air compressor to minimize environmental interference. The humidity inside the cavity was monitored using a temperature–humidity sensor to ensure stable environmental conditions. After the environment stabilized, 20 μL of each NAA solution—from low to high concentration—was dispensed onto the metamaterial surface using a calibrated micropipette. Afterward, the metamaterial was dried and allowed to cool to room temperature before being placed into the experimental instrument. To improve measurement accuracy, five points were selected for each sample, with ten spectral scans collected at each point. A total of 16 sample groups were tested, including 15 concentration-gradient samples and one bare metamaterial sample without any droplet addition, yielding 800 raw spectral datasets in total.

3 Experimental results and analysis

3.1 Analysis of terahertz transmission characteristics

By combining the L-shaped resonant metamaterial with terahertz spectroscopy detection method, the detection of trace NAA solution residues can be achieved. Fig. 5 shows the transmission spectral characteristics of different concentrations of NAA solutions. To minimize noise contributions at both low and high frequencies, the analysis frequency band was selected to be within the range of 1–3 THz. A total of 263 sampling points were finally preserved for subsequent model development. The enlarged images in Fig. 5 display the locally spectra around the two resonance frequencies. The results indicate that, as a result of the field-confinement characteristics of the metamaterial, the spectral detection exhibits a distinct amplitude response pattern: as the NAA concentration in the solution increases, the transmission peak amplitude decreases, and the transmission peak gradually red shifts.

3.2 Performance comparison and result analysis

To enhance the predictive performance for NAA residue determination, this work constructed a quantitative prediction model based on terahertz transmission spectroscopy data obtained through experiments, using Animated Oat Optimization (AOO)[19] algorithm and Support Vector Regression (SVR).[20] The effectiveness of SVR is strongly influenced by the choice of its hyperparameters. Conventional parameter-tuning approaches such as manual adjustment or grid search often suffer from dimensionality issues and may become trapped in suboptimal regions, limiting their ability to identify truly optimal hyperparameters.

The AOO algorithm, as an emerging intelligent optimization algorithm, has excellent global search ability and convergence efficiency, and can effectively find the optimal parameter combination in a complex search space. Therefore, by optimizing the hyperparameters through the AOO algorithm, the fitting accuracy and generalization ability of the model are improved, achieving the organic combination of parameter optimization and regression modeling between the two, enabling the automatic optimization of SVR hyperparameters, improving the modeling accuracy and generalization ability, and also enhancing the adaptability and practicability of the model in high-dimensional nonlinear data analysis.

To evaluate the capability of the proposed AOO-SVR approach for quantifying NAA concentrations from terahertz spectra, its performance was benchmarked against three other SVR models tuned with well-established optimization algorithms, including ant colony optimization (ACO),[21] simulated annealing (SA),[22] and genetic algorithms (GA).[23] Their predictive behavior was assessed using multiple statistical criteria, namely the correlation coefficient (R), root mean square error (RMSE), and mean absolute error (MAE). These metrics were employed to provide a comprehensive comparison of the fitting accuracy and generalization capability of each method.[24] The corresponding outcomes are displayed in Table 2 and Fig. 6.

The findings indicate that the AOO-SVR model delivers superior accuracy for quantitative analysis of NAA in terahertz spectra. It has the highest correlation coefficient (R) on both the training set and the test set, and the lowest error indicators

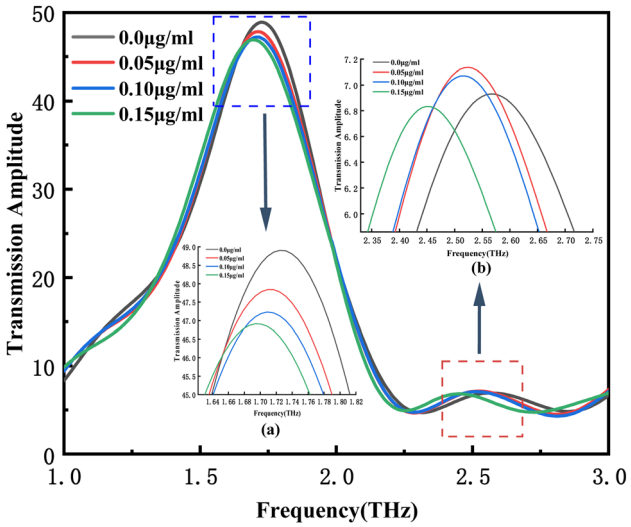

Fig. 5 Transmission spectra of the metamaterial sensor for different concentrations of NAA solution.

(RMSE and MAE), outperforming the SVR models optimized by ACO, SA and GA.

Terahertz spectral regression is characterized by strong feature correlation and nonlinear response behavior, making SVR performance highly sensitive to hyperparameter selection. AOO adopts a structured population learning strategy that balances global exploration and local exploitation through guidance from both elite solutions and population mean, which is well suited for continuous and sensitive parameter spaces. In contrast, GA-based methods may introduce parameter oscillations due to stochastic crossover and mutation, SA often suffers from slow convergence and dependence on initial states, and ACO is primarily designed for discrete or combinatorial optimization problems, limiting its efficiency in continuous spectral regression tasks. By maintaining stable convergence while avoiding premature local optima, AOO provides a more robust and physically consistent optimization framework for SVR modeling of terahertz spectral data.

In conclusion, the AOO-SVR model shows comprehensive superior performance when compared with others. The comparative findings substantiate that integrating AOO with SVR constitutes a robust modeling strategy for terahertz spectral analysis. The method exhibits notable improvements in predictive accuracy and generalization, highlighting both its methodological potential and practical relevance. Beyond enhancing residue detection performance, this framework also offers a promising direction for advancing optimization strategies in terahertz spectral data processing.

3.3 Feature extraction

The dimension of the original spectral data is 263, which is of a relatively high dimension. There may be strong redundancy and noise interference, limiting the potential for further improvement of the model. Therefore, in order to enhance the generalization ability and robustness of the model, this paper optimizes the dimension of the spectral data based on the original terahertz spectral data by using feature extraction algorithms such as Iteratively Retaining Informative Variables (IRIV),[25] Variable Iterative Spatial Shrinkage Approach (VISSA),[26] Competitive Adaptive Reweighted Sampling (CARS),[27] Mutual Information (MI),[28] and Recursive Feature Elimination (RFE).[29]

3.3.1 The feature extraction results of IRIV. Fig. 7 illustrates the IRIV-based feature screening procedure and its corresponding outcomes. To guarantee reliable and representative variable selection, the iteration was halted once the selected subsets became stable and further reductions in error were negligible. During iterative refinement, the algorithm progressively filters out variables with negligible influence on the model, ultimately retaining 36 key spectral features and effectively lowering data dimensionality. Fig. 7(a) shows the trend of the number of variables in each iteration, and Fig. 7(b) illustrates how the retained features are allocated following the screening process.

3.3.2 The feature extraction results of VISSA. Fig. 8 illustrates the workflow and outcomes of feature refinement using the VISSA method. Through a progressive compression of the spectral space, VISSA narrows down the candidate features and filters out components that provide limited analytical value, thus enhancing the robustness of the model and improving its prediction performance. Following the predefined iteration rules, the procedure ultimately preserved 160 informative spectral points. In Fig. 8(a), the variation in RMSECV before and after the VISSA-based refinement is compared, while Fig. 8(b)

Table 2 Evaluation of prediction effects of each model

		Training set			Test set		
Model	C, γ	R	RMSE	MAE	R	RMSE	MAE
ACO-SVR	$C = 562.1049$ $\gamma = 0.5802$	0.9996	1.3981×10^{-3}	1.3449×10^{-3}	0.9529	1.4508×10^{-2}	8.6304×10^{-3}
SA-SVR	$C = 0.2181$ $\gamma = 0.1026$	0.9474	1.4812×10^{-2}	7.9476×10^{-3}	0.9450	1.5576×10^{-2}	8.5175×10^{-3}
GA-SVR	$C = 682.0565$ $\gamma = 1.3408$	0.9997	1.4506×10^{-3}	1.4240×10^{-3}	0.9241	1.9801×10^{-2}	1.3729×10^{-2}
AOO-SVR	$\boldsymbol{C = 387.4154}$ $\boldsymbol{\gamma = 0.3875}$	**0.9995**	$\mathbf{1.3848 \times 10^{-3}}$	$\mathbf{1.3304 \times 10^{-3}}$	**0.9578**	$\mathbf{1.3663 \times 10^{-2}}$	$\mathbf{7.3403 \times 10^{-3}}$

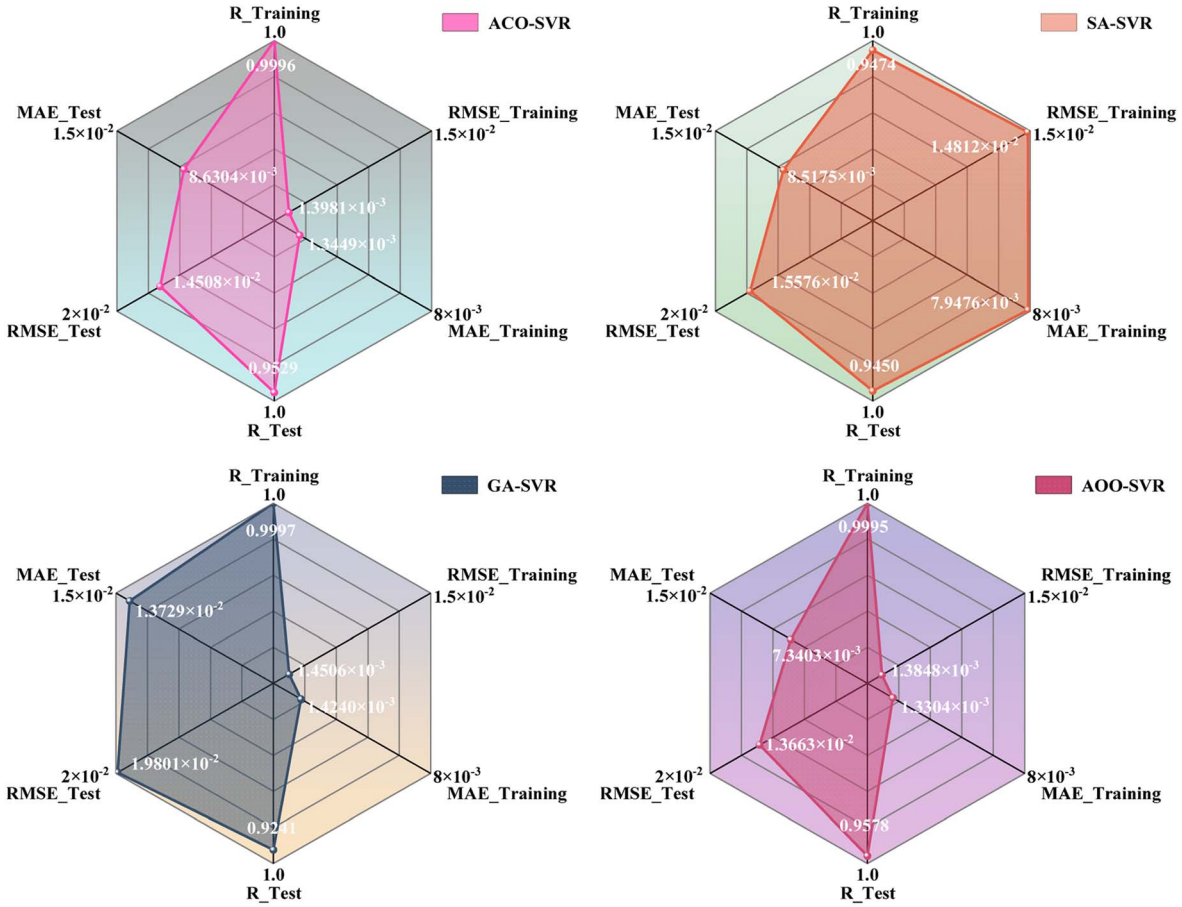

Fig. 6 Evaluation of Prediction effects of each model.

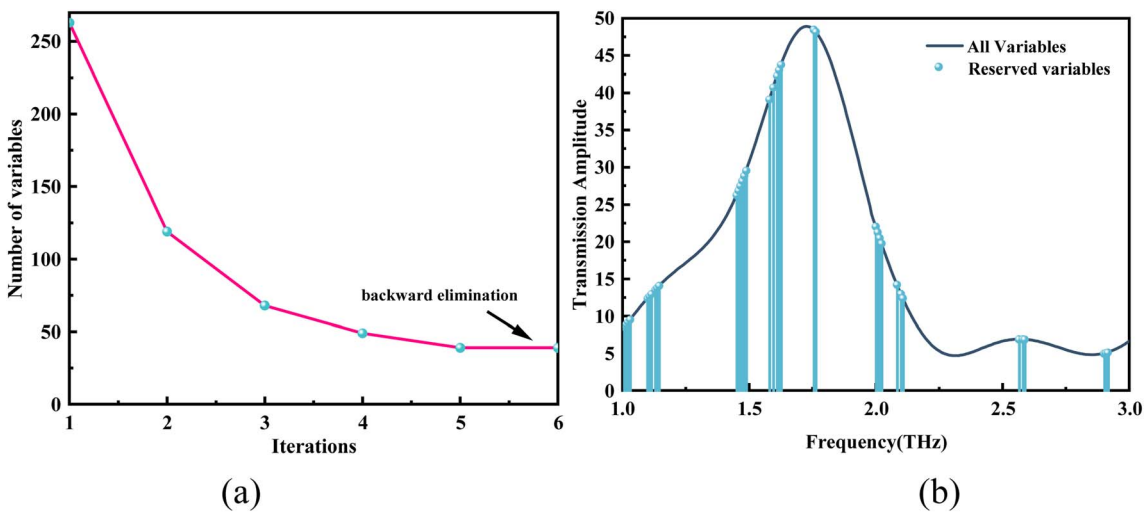

Fig. 7 (a) Evolution of IRIV-derived variable subsets; (b) final layout of the retained spectral variables.

visualizes where the retained spectral components lie along the frequency domain.

3.3.3 The feature extraction results of CARS. Fig. 9 illustrates how the CARS algorithm identifies and filters informative spectral variables, along with the corresponding outcome of this screening procedure. CARS simulates the "survival competition" mechanism and, during the iterative process, combines Monte Carlo sampling and regression coefficient weighting strategies to gradually eliminate the feature variables that contribute less to the model, thereby optimizing the sub-set

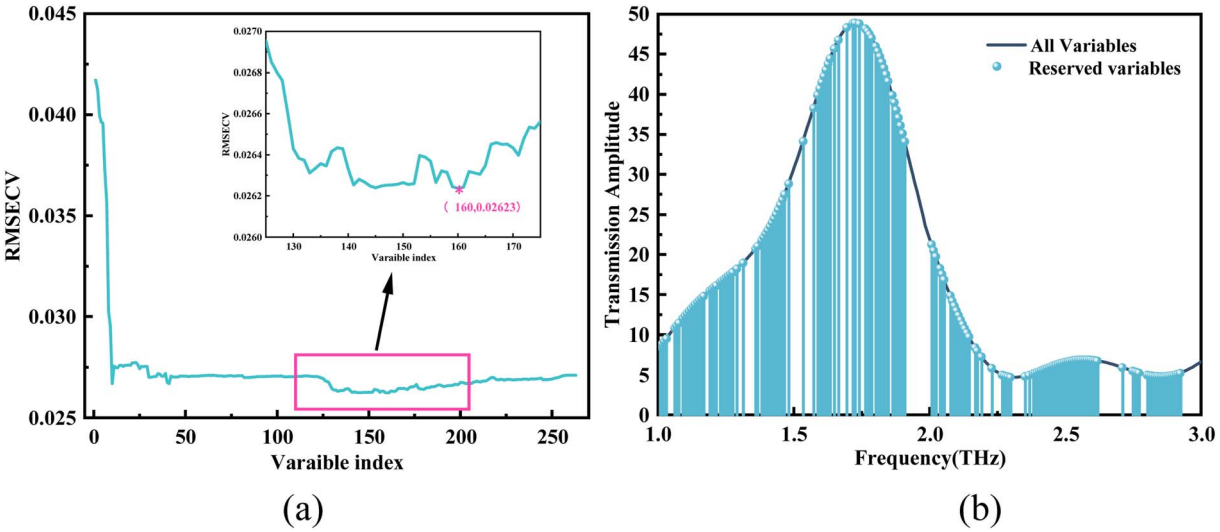

Fig. 8 (a) Comparison of RMSECV for VISSA feature extraction; (b) distribution of feature variables.

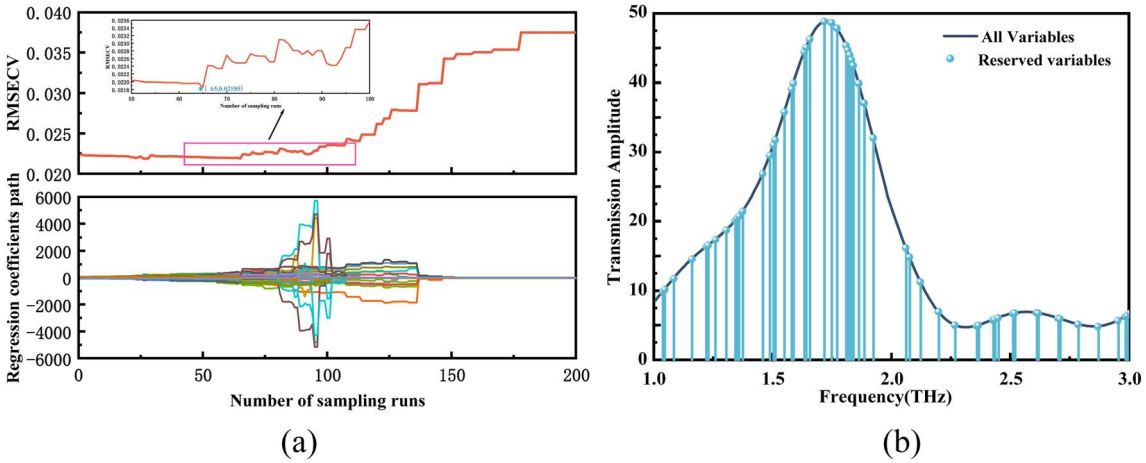

Fig. 9 (a) Output of the CARS-based variable screening; (b) spatial arrangement of the selected variables.

structure of variables. Fig. 9(a) shows the regression coefficient paths and RMSECV changes of the CARS algorithm under different number of runs. The results indicate that when the number of runs is 65, the RMSECV is the lowest, at 0.02185, and at this point, 55 variables are retained. Fig. 9(b) presents the distribution of feature variables.

3.3.4 The feature extraction results of MI. Fig. 10 presents the process and results of feature variable selection based on the MI algorithm. The MI algorithm measures the importance of variables by calculating the information correlation between each variable and the target variable, thereby sorting and selecting the bands. In this paper, the full-band spectral data is used as the initial variable set, and the top 8 variables with higher mutual information values are selected as significant features. Fig. 10(a) shows the mutual information values of different variables; Fig. 10(b) the positioning of the MI-selected features across the spectrum.

3.3.5 The feature extraction results of RFE. Fig. 11 displays how the RFE method filters and retains informative spectral components throughout its iterative procedure. RFE trains the base SVR model and gradually eliminates the variables with lower contribution according to the feature weights, iteratively optimizing the subset of variables to enhance the prediction performance and generalization ability of the model. The performance of each iteration model is evaluated using 5-fold cross-validation, and finally 182 key variables are selected. Fig. 11(a) compares the cross-validation error of the model prior to and following RFE refinement, while Fig. 11(b) illustrates how the retained spectral components are arranged along the frequency axis after the band selection.

3.4 Performance evaluation of the AOO-enhanced SVR model

3.4.1 Analysis of feature-reduced modeling outcomes. Table 3 and Fig. 12 summarize the predictive behavior of the

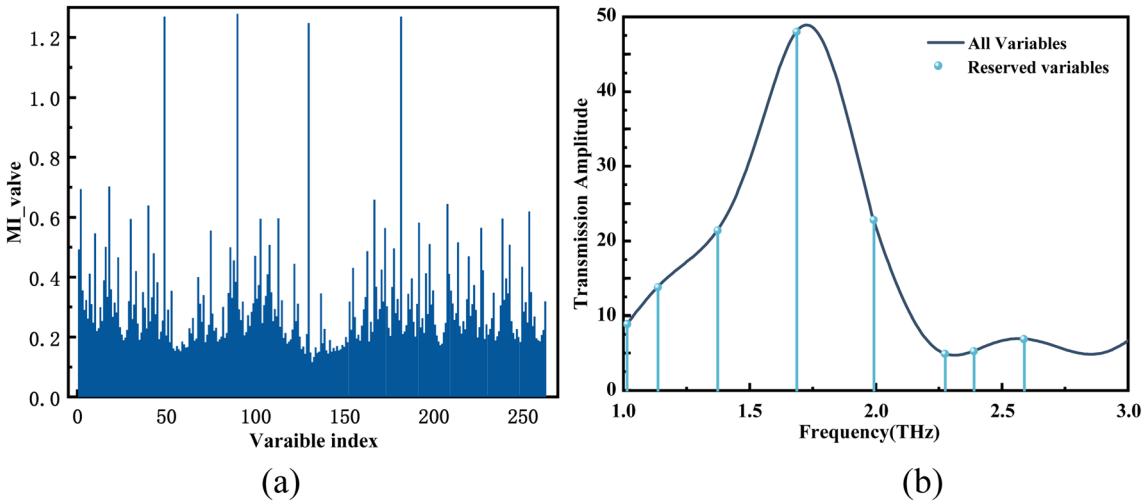

Fig. 10 (a) Mutual information values of different variables; (b) distribution of feature variables.

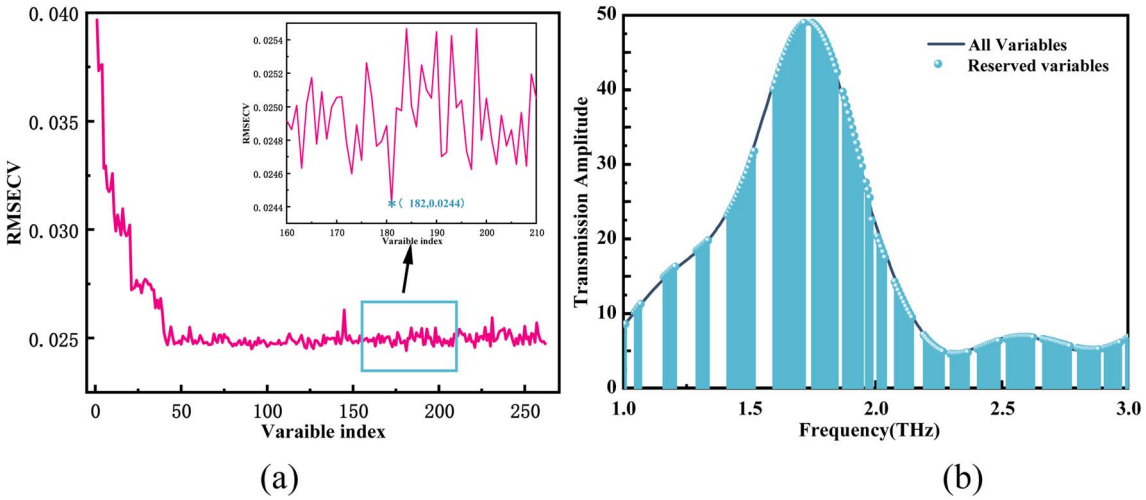

Fig. 11 (a) RMSECV comparison situation; (b) feature variable distribution situation.

AOO-SVR model when built on feature sets generated by different extraction strategies. As can be seen from the comparative outcomes, the AOO-SVR model after being filtered by IRIV, CARS and RFE feature extraction methods has shown a certain degree of optimization in all indicators. However, VISSA and MI have slightly decreased in all indicators. The possible reason is that VISSA and MI failed to fully retain the collaborative information of the spectrum in feature selection, resulting in information loss and decreased generalization ability. Overall, the model after RFE feature extraction performed the best. After feature refinement, the correlation coefficient increased to 0.9715, while the RMSE and MAE dropped to 1.1274×10^{-2} and 5.5496×10^{-3}, respectively. These improvements indicate that an appropriate variable-screening strategy effectively removes irrelevant information, reduces model redundancy, and strengthens the extraction of essential spectral cues. As a result, both the predictive precision and the robustness of the regression model are noticeably enhanced, demonstrating its stronger applicability in quantitative analysis.

The comparative evaluation shows that the subset retained by RFE allows the AOO-SVR model to reach its best predictive performance. The reason why RFE performed better than IRIV and CARS in this study might be: ① RFE exploits the SVR-assigned weights to prioritize input variables and evaluates how the model behaves as less informative components are progressively removed. It can effectively remove the bands that do not contribute to the model or have high redundancy while retaining the key bands. ② In contrast, although IRIV can gradually eliminate irrelevant variables, its initial random screening is prone to be interfered by noise; CARS relies on Monte Carlo sampling and regression coefficient paths, and is likely to retain some redundant features when there is high collinearity in the spectral bands. Therefore, RFE can maximize the improvement of the model's prediction accuracy and

Table 3 Comparison of modeling performance of AOO-SVR under different feature sets

			Training set			Test set		
Model	Variables numbers	C, γ	R_P	RMSE	MAE	R_P	RMSE	MAE
AOO-SVR	263	$C = 387.4154$ $\gamma = 0.3875$	0.9995	1.3848×10^{-3}	1.3304×10^{-3}	0.9578	1.3663×10^{-2}	7.3403×10^{-3}
IRIV-AOO-SVR	36	$C = 147.0807$ $\gamma = 0.4865$	0.9867	7.4384×10^{-3}	2.8079×10^{-3}	0.9633	1.2802×10^{-2}	6.7069×10^{-3}
VISSA-AOO-SVR	160	$C = 479.5131$ $\gamma = 0.6804$	0.9996	1.3801×10^{-3}	1.3183×10^{-3}	0.9536	1.4288×10^{-2}	7.5423×10^{-3}
CARS-AOO-SVR	55	$C = 288.5550$ $\gamma = 1.7589$	0.9996	1.3800×10^{-3}	1.3249×10^{-3}	0.9596	1.3284×10^{-2}	6.9712×10^{-3}
MI-AOO-SVR	8	$C = 344.2833$ $\gamma = 12.4456$	0.9995	1.4238×10^{-3}	1.3831×10^{-3}	0.9375	1.6561×10^{-2}	1.0099×10^{-2}
RFE-AOO-SVR	**182**	$\boldsymbol{C = 5.8465}$ $\boldsymbol{\gamma = 0.3151}$	**0.9918**	$\mathbf{5.8684 \times 10^{-3}}$	$\mathbf{2.0673 \times 10^{-3}}$	**0.9715**	$\mathbf{1.1274 \times 10^{-2}}$	$\mathbf{5.5496 \times 10^{-3}}$

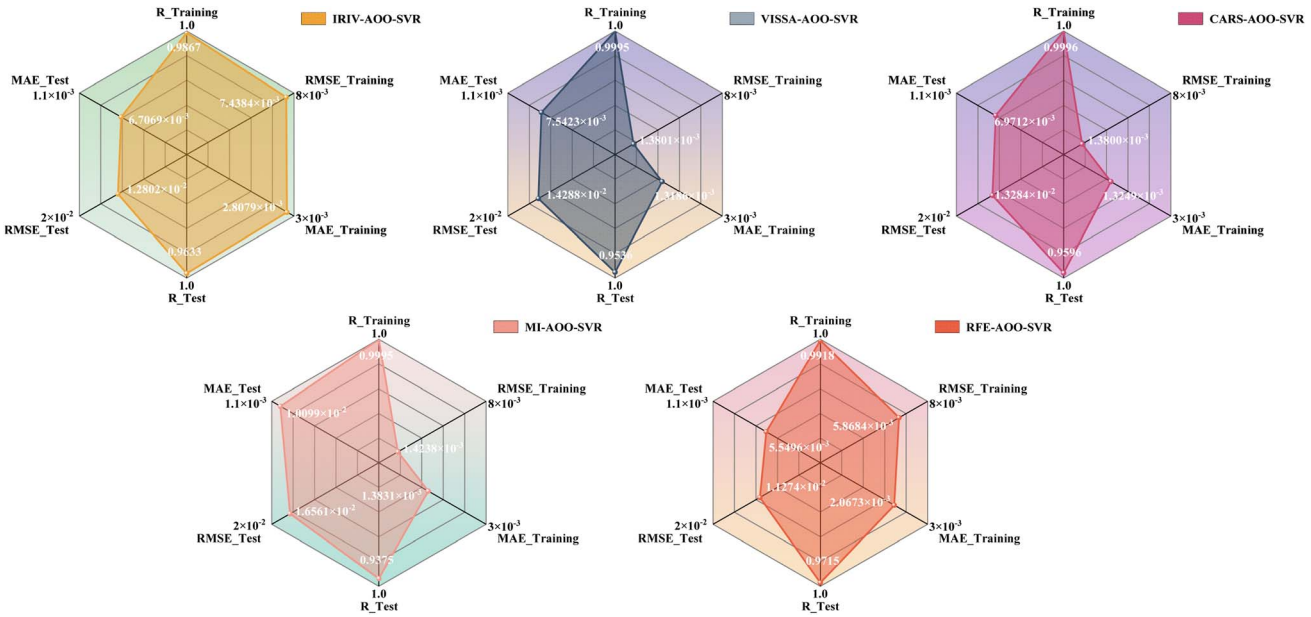

Fig. 12 Performance comparison of models built with various feature subsets.

robustness while reducing redundancy and suppressing overfitting.

3.4.2 Calculation of the minimum detectable concentration. To examine how well the AOO-SVR approach responds to low-level signals in real scenarios, the detection limit (LOD) was estimated using the feature-reduced dataset. The detection limit serves as a key metric reflecting how effectively a quantitative model can recognize signals approaching the lowest measurable concentration of the analyte. Estimating the LOD provides additional evidence that the model can reliably handle trace-level NAA measurements.[30] In this work, the LOD was determined using the three-sigma criterion, where the LOD is estimated by taking three times the standard deviation of the prediction outputs and normalizing it by the regression slope of the model. This approach provides a statistically grounded and practically meaningful estimate of the lowest detectable level. The calculation formula is:[31]

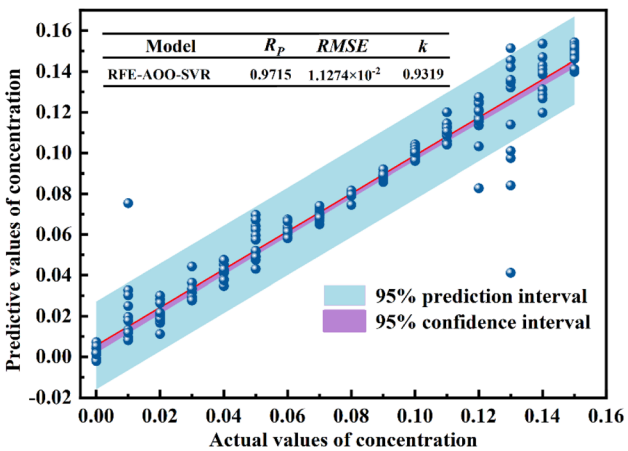

Fig. 13 The fitting graph between the actual values and the predicted values.

Table 4 Comparison of the proposed method with representative traditional pesticide residue detection methods

Testing methods	The objects of detection	LOD	Reference
GC-MS/MS	147 Pesticide residues	0.050 mg kg^{-1}	32
HPLC	Captan, triclopyr and mesotrione	162.5 mg kg^{-1}	33
FTIR	Boscalid	3.06 μg cm^{-2}	34
SERS	Acetamiprid	1 mg kg^{-1}	35
Terahertz metamaterials	**NAA**	**0.036 μg mL^{-1}**	**This work**

$$\mathrm{LOD} = \frac{3\sigma}{k}$$

Fig. 13 shows the fitting graph of the predicted values of the RFE-AOO-SVR model and the true values. According to Formula, the LOD of the model is calculated to be 0.036 μg mL^{-1}. The AOO-SVR model after feature extraction shows a better detection limit level, indicating that this method has certain sensitivity in the detection of low-concentration NAA residues.

To better contextualize the detection performance of the proposed approach, a comparison with representative traditional pesticide residue detection methods reported in the literature is provided, as summarized in Table 4.

The proposed terahertz metamaterial-based sensing method achieves a detection limit that is comparable to those of commonly used analytical and spectroscopic techniques for pesticide residue analysis. In addition, by combining metamaterial-enhanced terahertz spectral responses with regression modeling, the proposed method demonstrates a competitive sensing capability for trace-level NAA detection, indicating its potential as an alternative quantitative analysis approach under controlled detection conditions.

4 Conclusion

This study proposes a terahertz metamaterial sensor based on an L-type resonant structure, which is applied in the non-destructive detection of NAA residues. A high-performance quantitative modeling method integrating the AOO optimization algorithm and SVR is presented. By comparing with traditional intelligent optimization algorithms such as PSO-SVR, SA-SVR, and GA-SVR, AOO-SVR demonstrates superior predictive performance in terms of R, RMSE, and MAE. Further, by combining five feature extraction algorithms, the prediction accuracy and generalization ability of the model are effectively improved. Among them, the RFE-AOO-SVR model achieves the best performance in all indicators, with the lowest LOD, indicating stronger feature selection ability and modeling adaptability. In conclusion, the detection framework integrating the L-type resonant metamaterial sensor and the RFE-AOO-SVR intelligent modeling method not only realizes high-sensitivity quantitative analysis of trace NAA residues, but also verifies the feasibility and superiority of the AOO optimization algorithm in the field of spectral detection, providing a practical and expandable research path for terahertz spectroscopy technology in the rapid detection of pesticide residues.

In practical applications, the proposed method is intended for pesticide residue analysis in agricultural samples after standardized pretreatment, where extracted analytes are subsequently measured under a controlled thin-layer configuration. Meanwhile, to further demonstrate the practical applicability of the proposed method, future work will focus on validating the terahertz metamaterial sensor and AOO-SVR model using representative real sample matrices (*e.g.*, fruit or vegetable extracts spiked with NAA), so as to assess matrix interference and enhance the reliability of the system under realistic detection conditions.

Author contributions

Xiaodong Mao: writing – original draft, experiment, data processing. Zhikai Huang: experiment, visualization. Tao Yang: code writing. Jun Hu: investigation, writing – review and editing, experimental scheme design, formal analysis.

Conflicts of interest

We declare that we have no financial and personal relationships with other people or organizations that can inappropriately influence our work, there is no professional or other personal interest of any nature or kind in any product, service and/or company that could be construed as influencing the position presented in, or the review of, the manuscript. Xiaodong Mao, Zhikai Huang, Tao Yang, Jun Hu declare that they have no conflicts of interest.

Data availability

Data underlying the results presented in this paper are not publicly available at this time but may be obtained from the authors upon reasonable request.

Acknowledgements

National Youth Natural Science Foundation of China (Grant No. 32302261); Jiangxi Ganpo Talented Support Plan -Young Science and Technology Talent Lift Project (Grant No. 2023QT04); Jiangxi Province Natural Science Foundation Project (20242BAB202053).

References

1 R. J. Hill, D. R. King, R. Zollinger, *et al.*, 1-Naphthaleneacetic acid (NAA) reduces sucker growth in European hazelnut (Corylus avellana L.), *HortScience*, 2021, **56**(12), 1594–1598.

2 S. W. Chung, Y. J. Jang, C. K. Lim, *et al.*, Effects of 1-Naphthaleneacetic acid on the panicle and fruit characteristics of â Irwinâ mango trees, *Hortic. Sci. Technol.*, 2023, **41**(4), 361–369.

3 G. Ma, L. Zhang, K. Murakami, *et al.*, Effects of Postharvest Treatment with 1-Naphthaleneacetic Acid on Chlorophyll and Carotenoid Metabolism in Citrus Fruit, *Hortic. J.*, 2023, **92**(4), 393–401.

4 W. Qiu, J. Chen, Y. Hua, *et al.*, Method development, multi-residue determination, and dietary exposure risk assessment of plant growth regulators in homologous materials of medicine and food, *Environ. Monit. Assess.*, 2024, **196**(11), 1039.

5 K. HÄ c-Wydro and M. FlasiÅ, ski, The studies on the toxicity mechanism of environmentally hazardous natural (IAA) and synthetic (NAA) auxinâ€"the experiments on model Arabidopsis thaliana and rat liver plasma membranes[J], *Colloids Surf., B*, 2015, **130**, 53–60.

6 G. Helmy, S. Ahmed and S. Mahrous, Evaluation of synthetic plant growth regulators residues in fruits and vegetables and health risk assessment in Giza, Egypt, *J. Soil Sci. Agric. Eng.*, 2015, **6**(9), 1075–1089.

7 Standardization Administration of China, *GB 2763-2021 Maximum Residue Limits of Pesticides in Food [S]*, Beijing, China Standards Press, 2021.

8 X. C. Zhang, and J. Xu, *Introduction to THz Wave photonics[M]*, New York, Springer, 2010.

9 M. Koch, D. M. Mittleman, J. Ornik, *et al.*, Terahertz time-domain spectroscopy, *Nat. Rev. Methods Primers*, 2023, **3**(1), 48.

10 P. A. Banks, E. M. Kleist and M. T. Ruggiero, Investigating the function and design of molecular materials through terahertz vibrational spectroscopy, *Nat. Rev. Chem.*, 2023, **7**(7), 480–495.

11 L. Zhang, M. Zhang and A. S. Mujumdar, Terahertz spectroscopy: a powerful technique for food drying research, *Food Rev. Int.*, 2023, **39**(3), 1733–1750.

12 C. Han, F. Qu, X. Wang, *et al.*, Terahertz spectroscopy and imaging techniques for herbal medicinal plants detection: a comprehensive review, *Crit. Rev. Anal. Chem.*, 2024, **54**(7), 2485–2499.

13 W. Wang, K. Sun, Y. Xue, *et al.*, A review of terahertz metamaterial sensors and their applications, *Opt. Commun.*, 2024, **556**, 130266.

14 J. Li, J. Chen, D. Yan, *et al.*, A review: Active tunable terahertz metamaterials, *Adv. Photonics Res.*, 2024, **5**(7), 2300351.

15 X. Wei, C. Ren, B. Liu, *et al.*, The theory, technology, and application of terahertz metamaterial biosensors: A review, *Fundam. Res.*, 2025, **5**(2), 571–585.

16 F. Ahmed, M. A. Azim and A. Zubair, High sensitivity terahertz metamaterial sensor for trace pesticide detection, *RSC Adv.*, 2025, **15**(26), 20530–20541.

17 N. M. Chowdhury, M. M. Soliman, A. M. Alenezi, *et al.*, Sensitivity detection of imidacloprid pesticide using a metasurface sensor in THz spectrum regime, *Eng. Sci. Technol. Int. J.*, 2024, **57**, 101801.

18 X. Du, Z. Yu, X. Du, *et al.*, Study on absorption enhancement mechanism and application of terahertz combined metamaterial, *IEEE Sens. J.*, 2024, **24**(19), 29953–29961.

19 R. B. Wang, R. B. Hu, F. D. Geng, *et al.*, The Animated Oat Optimization Algorithm: A nature-inspired metaheuristic for engineering optimization and a case study on Wireless Sensor Networks, *Knowl. Base Syst.*, 2025, 113589.

20 M. Awad, R. Khanna, M. Awad, *et al. Support Vector regression*, Efficient Learning Machines: Theories, Concepts, and Applications for Engineers and System Designers, 2015, pp. 67–80.

21 M. Dorigo, M. Birattari and T. Stutzle, Ant colony optimization, *IEEE Comput. Intell. Mag.*, 2007, **1**(4), 28–39.

22 C. Venkateswaran, M. Ramachandran, K. Ramu, *et al.*, Application of simulated annealing in various field, *Mater. Charact.*, 2022, **1**(1), 01–08.

23 S. Mirjalili, and S. Mirjalili, *Genetic algorithm*, Evolutionary Algorithms and Neural Networks: Theory and Applications, 2019, pp. 43–55.

24 H. Zhang, J. Gao, L. Tan, *et al.*, Research on the Application of Terahertz Technology in Detecting Additives in Milk Powder, *Food Anal. Methods*, 2025, **18**(3), 398–415.

25 Y. H. Yun, W. T. Wang, M. L. Tan, *et al.*, A strategy that iteratively retains informative variables for selecting optimal variable subset in multivariate calibration, *Anal. Chim. Acta*, 2014, **807**, 36–43.

26 B. Deng, Y. Yun, Y. Liang, *et al.*, A novel variable selection approach that iteratively optimizes variable space using weighted binary matrix sampling, *Analyst*, 2014, **139**(19), 4836–4845.

27 H. Li, Y. Liang, Q. Xu, *et al.*, Key wavelengths screening using competitive adaptive reweighted sampling method for multivariate calibration, *Anal. Chim. Acta*, 2009, **648**(1), 77–84.

28 H. Gong, Y. Li, J. Zhang, *et al.*, A new filter feature selection algorithm for classification task by ensembling pearson correlation coefficient and mutual information, *Eng. Appl. Artif. Intell.*, 2024, **131**, 107865.

29 H. Jeon and S. Oh, Hybrid-recursive feature elimination for efficient feature selection, *Appl. Sci.*, 2020, **10**(9), 3211.

30 G. Donati, The Case of the Limit of Detection, *Braz. J. Anal. Chem.*, 2022, **9**(36), 8–9.

31 J. Hu, C. Zhan, Q. Wang, *et al.*, Research on highly sensitive quantitative detection of aflatoxin b2 solution based on thz metamaterial enhancement, *Spectrochim. Acta, Part A*, 2023, **300**, 122809.

32 C. Ji, L. Xiao, X. Wang, *et al.*, Simultaneous Determination of 147 Pesticide Residues in Traditional Chinese Medicines by GC–MS/MS, *ACS Omega*, 2023, **8**(31), 28663–28673.

33 J. Brinco, A. Branco Ribeiro, J. Cardoso, *et al.*, Monitoring pesticides in post-consumer containers by GC/TOFMS and HPLC/DAD after the triple rinse method, *Int. J. Environ. Anal. Chem.*, 2024, **104**(4), 867–878.
34 J. Brinco, A. Branco Ribeiro, J. Cardoso, *et al.*, Monitoring pesticides in post-consumer containers by GC/TOFMS and HPLC/DAD after the triple rinse method, *Int. J. Environ. Anal. Chem.*, 2024, **104**(4), 867–878.
35 G. Lv, D. Shan, Y. Ma, *et al.*, In-situ quantitative prediction of pesticide residues on plant surface by ATR-FTIR technique coupled with chemometrics, *Spectrochim. Acta, Part A*, 2024, **305**, 123432.